Title: Single-unit-cell layer established Bi_2WO_6 3D hierarchical architectures: Efficient adsorption, photocatalysis and dye-sensitized photoelectrochemical performance

Authors: Hongwei Huang, Ranran Cao, Shixin Yu, Kang Xu, Weichang Hao, Yonggang Wang, Fan Dong, Tierui Zhang, Yihe Zhang

PII: S0926-3373(17)30733-6
DOI: http://dx.doi.org/doi:10.1016/j.apcatb.2017.07.084
Reference: APCATB 15916

To appear in: *Applied Catalysis B: Environmental*

Received date: 24-1-2017
Revised date: 2-5-2017
Accepted date: 27-7-2017

Please cite this article as: Hongwei Huang, Ranran Cao, Shixin Yu, Kang Xu, Weichang Hao, Yonggang Wang, Fan Dong, Tierui Zhang, Yihe Zhang, Single-unit-cell layer established Bi2WO6 3D hierarchical architectures: Efficient adsorption, photocatalysis and dye-sensitized photoelectrochemical performance, Applied Catalysis B, Environmentalhttp://dx.doi.org/10.1016/j.apcatb.2017.07.084

Single-unit-cell layer established Bi_2WO_6 3D hierarchical architectures: Efficient adsorption, photocatalysis and dye-sensitized photoelectrochemical performance

Hongwei Huang[a,*], Ranran Cao[a], Shixin Yu[a], Kang Xu[b], Weichang Hao[b], Yonggang Wang[c], Fan Dong[d], Tierui Zhang[e], Yihe Zhang[a,*]

[a]*Beijing Key Laboratory of Materials Utilization of Nonmetallic Minerals and Solid Wastes, National Laboratory of Mineral Materials, School of Materials Science and Technology, China University of Geosciences, Beijing 100083, China*

[b]*Center of Materials Physics and Chemistry and Department of Physics, Beihang University, Beijing 100191, China*

[c]*High Pressure Science and Engineering Centre, University of Nevada Las Vegas, Las Vegas 89154, Nevada, USA*

[d]*Chongqing Key Laboratory of Catalysis and Functional Organic Molecules, College of Environmental and Bio-logical Engineering, Chongqing Technology and Business University, Chongqing, 400067, China*

[e]*Key Laboratory of Photochemical Conversion and Optoelectronic Materials, Technical Institute of Physics and Chemistry, Chinese Academy of Sciences, Beijing 100190, China*

Corresponding Author

**E-mail: hhw@cugb.edu.cn; zyh@cugb.edu.cn.*

Graphical Abstract

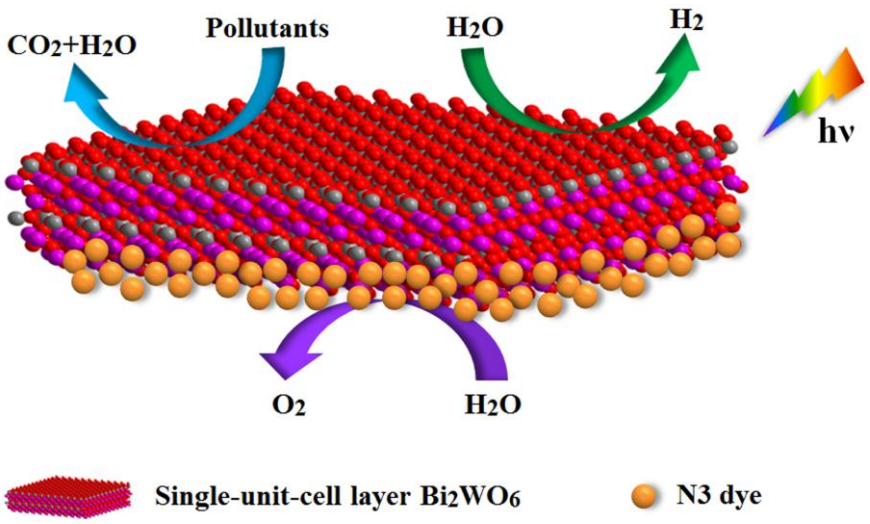

Highlights

- Single-unit-cell layer established 3D Bi_2WO_6 by SDBS-assisted assembled strategy.
- It shows a strong selectivity for adsorption on positively-charged organic dyes.
- It presents highly enhanced photocatalytic activity for degradation and H_2 evolution.
- Systematic photoelectrochemical experiments confirm the promoted charge separation.
- Single-unit-cell 3D Bi_2WO_6 is a promising dye-sensitized photoanode for ORR.

ABSTRACT: Single-layer catalysis sparks huge interests and gains widespread attention owing to its high activity. Simultaneously, three-dimensional (3D) hierarchical structure can afford large surface area and abundant reactive sites, contributing to high efficiency. Herein, we report an absorbing single-unit-cell layer established Bi_2WO_6 3D hierarchical architecture fabricated by a sodium dodecyl benzene sulfonate (SDBS)-assisted assembled strategy. The DBS^- long chains can adsorb on the $(Bi_2O_2)^{2+}$ layers and hence impede stacking of the layers, resulting in the single-unit-cell layer. We also uncovered that SDS with a shorter chain is less effective than SDBS. Due to the sufficient exposure of surface O atoms, single-unit-cell layer 3D Bi_2WO_6 shows strong selectivity for adsorption on multiform organic dyes with different charges. Remarkably, the single-unit-cell layer 3D Bi_2WO_6 casts profoundly enhanced photodegradation activity and especially a superior photocatalytic H_2 evolution rate, which is 14-fold increase in contrast to the bulk Bi_2WO_6. Systematic photoelectrochemical characterizations disclose that the substantially elevated carrier density and charge separation efficiency take responsibility for the strengthened photocatalytic performance. Additionally, the possibility of single-unit-cell layer 3D Bi_2WO_6 as dye-sensitized solar cells (DSSC) has also been attempted and it was manifested to be a promising dye-sensitized photoanode for oxygen evolution reaction (ORR). Our work not only furnish an insight into designing single-layer assembled 3D hierarchical architecture, but also offer a multi-functional material for environmental and energy applications.

KEYWORDS: *single-unit-cell layer, 3D hierarchical architecture, Bi_2WO_6, photocatalysis, dye-sensitized photoanode*

1. Introduction

Single-layer or few-layers two-dimensional (2D) materials, such as graphene, boron nitride (BN), graphitic carbon nitride (g-C_3N_4) and transition metal dichalcogenides, have sparked considerable interests in the fields of catalysis [1], electronics [2] and energy generation and storage [3]. Especially, they cast great potentials in photocatalysis and photoelectrochemistry, as the ultrathin thickness allows the photogenerated charge carriers to breezily emigrate from the inside to surface, thus resulting in a decreased bulk recombination rate and resultant improved photocatalytic and/or photoelectrochemical performance based on the diffusion time formula of $t=d^2/k^2D$ (k, D and d indicate a constant, diffusion coefficient of electron-hole pairs and the particle size, respectively) [4].

Layered bismuth-based (LBB) semiconductor photocatalytic materials have recently gained widespread attention because of their high photo-oxidation ability, high photo and chemical stability and especially abundant structural diversity [5-7]. These LBB semiconductors characterized by $(Bi_2O_2)^{2+}$ layers and interlayer ions or polyhedra, comprise Sillén structured BiOX (X=Cl, Br, I) [8-11], Aurivillius structured Bi_2MoO_6, Bi_2WO_6, and Bi_2SiO_5 [12-15], Sillén-Aurivillius structured Bi_4NbO_8X (X=Cl, Br) [16,17], pyrochlore-structure Bi_2MNbO_7 (M = Al, Ga, In, Fe, and Sm) [18], and a series of newly discovered LBB photocatalysts by our group, including Sillén structure-related $Bi_2O_2[BO_2(OH)]$ [19], $Bi_2O_2(OH)(NO_3)$ [20], Bi_2MO_4Cl (M=Eu, Gd) [21], and $MBiO_2N$ (M=Sr, Ba; N=Cl, Br) [22,23]. As the simplest Aurivillius-type compound and simultaneously containing the WO_6 perovskite group, Bi_2WO_6 shows promising prospect for photocatalytic purify of organic contaminants, water splitting into H_2 evolution and CO_2

reduction. Though numerous efforts have been made to improve the photocatalytic performance of Bi_2WO_6, such as ion doping [24,25], heterojunction fabrication [26-28], noble metal deposition [29,30], etc., the activity enhancement is still limited. Lately, Br^- ion modified monolayer Bi_2WO_6 was prepared through a cetyltrimethylammonium bromide (CTAB)-assisted hydrothermal process, and the adsorption on different dyes is investigated [31]. Besides, Liang, et. al. reported the synthesis of single-unit-cell Bi_2WO_6 layers by using oleate as capping agent and demonstrated their efficient photocatalytic activity for CO_2 reduction into methanol [32]. Though monolayer or few-layers of Bi_2WO_6 are achieved in the above-mentioned work, the products are composed of dispersed nanosheets, which suffer from limited surface area and/or light absorption compared to three dimensional (3D) configuration. Considering the advantages of ultrathin nanosheets and 3D structure, developing Bi_2WO_6 3D hierarchical architectures assembled by single-layer nanosheets may be highly appealing and of significance. Besides, in addition to photocatalytic property in environmental and energy field, exploration of more interesting applications of single-layer Bi_2WO_6 is more challenging and alluring.

Herein, we develop an anionic surfaceactive agent sodium dodecyl benzene sulfonate (SDBS)-assisted strategy for fabricating single-unit-cell layer assembled Bi_2WO_6 3D hierarchical architectures. The DBS^- long chains can adsorb on the $(Bi_2O_2)^{2+}$ layers and hence impede stacking of the layers. For confirmation, the SDBS concentration and a shorter-chain sodium dodecyl sulfonate (SDS) are also attempted and compared. DFT and experimental results co-disclose that the exposed surface atoms of single-unit-cell layer Bi_2WO_6 are O atoms from Bi-O and W-O groups, which thus enables it a strong selective adsorption on positively-charged dyes. The photocatalytic tests reveal that the

single-unit-cell layer 3D Bi_2WO_6 shows highly enhanced photocatalytic degradation and H_2 evolution performance. Systematical photoelectrochemical characterizations are hence conducted to explain the enhanced photocatalytic activity. In addition, the single-unit-cell layer 3D Bi_2WO_6 was also investigated as a dye-sensitized solar cell (DSSC) and the results demonstrate that it may serve as a potential dye-sensitized photoanode for oxygen evolution reaction (ORR).

2. Experimental Section

2.1. Synthesis.

Chemicals of $Bi(NO_3)_3 \cdot 5H_2O$ (Sigma-Aldrich), $Na_2WO_4 \cdot 2H_2O$ (Sigma-Aldrich), sodium dodecyl benzene sulfonate (SDBS, Beijing Chemical Co., Ltd) and sodium dodecyl sulfate (SDS, Beijing Chemical Co., Ltd) are obtained from commercial sources and used as received. Bulk Bi_2WO_6 and single-unit-cell 3D Bi_2WO_6 samples are synthesized by a one-pot hydrothermal process. In a typical synthesis of single-unit-cell layer Bi_2WO_6, 2 mmol $Bi(NO_3)_3 \cdot 5H_2O$, 2 mmol $Na_2WO_4 \cdot 2H_2O$, and 0.1 mmol SDBS are dissolved in 30 ml distilled water and put in a 50 ml Teflon-lined stainless autoclave. Then, they are heated at 180 ℃ for 24 h. After cooling to room temperature, the products were collected by repeated centrifugation with ethanol and n-hexane and then dried at 80 ℃ for 5 h. Bulk Bi_2WO_6 is prepared by the same procedure without adding SDBS. The samples obtained with adding 0.2 mmol SDBS, 1 mmol SDBS and 0.1 mmol sodium dodecyl sulfate (SDS) for replacing 0.1 mmol SDBS are denoted as Bi_2WO_6-SDBS1, Bi_2WO_6-SDBS2 and SUC-Bi2WO6, respectively.

2.2 Characterization.

The room temperature X-ray Absorption Fine Structure (XAFS) data on the Bi L3-edge (13.419 keV) of Bulk Bi_2WO_6 and single-unit-cell Bi_2WO_6 were measured at the 16BM-D station of the High-Pressure Collaborative Access Team (HPCAT) at the Advanced Phonon Source of Argonne National Laboratory. The data were processed and fitted with the program Athena [33]. X-ray diffraction (XRD) was conducted with the 2θ between 10 and 70 degrees on a D8 Advance X-ray diffractometer (Bruker AXS, Germany) with Cu Kα radiation (λ= 1.5418Å). The scanning step width of 0.02° and the scanning rate of 0.2° S^{-1} were applied. Raman spectra in the range between 200 and 1000 cm^{-1} were obtained by a Raman-11 spectrometer (Nanophoton, Japan). X-ray photoelectron spectroscopy (XPS) was performed on a VGMK II X-ray photoelectron spectrometer. Scanning electron microscopy (SEM, S-4800 Hitachi, Japan) and transmission electron microscopy (TEM, JEM-2100 JEOL, Japan) are employed to study the morphology and microstructure of the products. BET specific surface area is determined by nitrogen adsorption method with a Micromeritics 3020 instrument (USA). UV-vis diffuse reflectance spectra (DRS) with range 200-800 nm were carried out on a Varian Cary 5000 UV-vis spectrophotometer (USA). Thermogravi-metric (TG) curves of Bi_2WO_6 and SUC-Bi_2WO_6 with range of 20-600℃ and heating rate of 20℃ min^{-1} are collected on a Labsys TGDTA16 (SETARAM, France) thermal analyzer. A Varian 710-ES (Varian, Shanghai, China) inductively coupled plasma optical emission spectrometer (ICP-OES) with Sepex Certiprep standards was used to analyze the Pt content.

2.3 Adsorption and photodegradation experiments.

Adsorption experiment was conducted in darkness with Rhodamine B (RhB, 0.01 mM), methylene blue (MB, 0.01 mM), methyl orange (MO, 0.01 mM) and phenol (10

mg/L) as targets. 50 mg of photocatalyst is totally dispersed in the above contaminant solutions (50 ml) with strong stirring, and then the suspension was taken and centrifugated for every 10 min. The concentration of these pollutants was determined by recording the absorption spectrum based on their absorbance bands. After 30 min adsorption experiment, the photocatalytic degradation performance of the photocatalysts was studied by irradiation of visible light (a 500 W xenon lamp, $\lambda > 420$ nm). The photochemical reactor in the current work is a 8-sites disc reactor that can simultaneously hold 8 quartz tubes with a 500 W tubular Xe lamp in the center, and the Xe lamp is encircled by eight 420 nm cutoff filters. The distance between Xe lamp and reaction solutions (quartz tubes) is 10 cm, and the average light intensity is determined to be about 18.2 mW/cm^2. The irradiation lasts for 60 min, and the supernatant was measured by the same spectroscopic method.

2.4 Active Species Trapping Experiments.

To inspect the active species generated in photocatalytic RhB degradation process of SUC-Bi_2WO_6, benzoquinone (1 mM BQ, Sigma-Aldrich), ethylenediaminetetraacetic acid disodium salt (1 mM EDTA-2Na, Xilong Chemical Co., Ltd), and isopropanol (1mM IPA, Aldrich) are used as the scavengers of superoxide radicals ($\bullet O_2^-$), holes (h^+), and hydroxyl radicals (•OH), respectively [11,15]. The procedure is similar to above photodegradation test with replacing RhB with scavengers.

2.5 Photocatalytic H_2 production.

Photocatalytic H_2 evolution experiments were conducted in a photoreactor (Pyrex glass) connected to aclosed-cycle gas circulation system with a 300 W Xe lamp as light source. Typically, 50 mg of photocatalyst powder was suspended in a mixed solution of

25 mL distilled water and 20 mL methanol. Then, 3 wt% Pt was photo-deposited in the above suspension from H_2PtCl_6 as cocatalyst, and the Pt content actually incorporated into SUC-Bi_2WO_6 was determined to be about 1.8 wt% by elemental analysis. The Pt particle size is about 10 nm, as revealed by the high-resolution SEM (Fig. S1). This suspension was bubbled by nitrogen for 30 min to remove dissolved oxygen prior to photocatalytic reaction. Afterward, the H_2 evolution test was carried out on an online photocatalytic reaction system (Labsolar-IIIAG), and analyzed by a gas chromatography (GC7900, Tianmei, Shanghai, TCD).

2.6 Photoelectrochemical tests.

Photocurrent measurements of Bulk Bi_2WO_6 and single-unit-cell Bi_2WO_6 were conducted in a three-electrode system with on an electrochemical system (CHI-660E, Shanghai, China). Saturated calomel electrodes (SCE), platinum wires and the Bi_2WO_6 films coated on ITO serve as reference electrode, counter electrode and working electrode, respectively. The electrolyte is 0.1 M Na_2SO_4 solution. Methylviologen dichloride ($MVCl_2$) was added in the photocurrent onset scans to insure the fast reaction kinetics at the electrode surface.

2.7 Assembly and testing of dye-sensitized solar cells.

Bi_2WO_6 pastes were first prepared by the following method: 200 mg Bi_2WO_6 was successively mixed with 2 ml of 10 wt% ethyl cellulose ethanol solution and 1.8 ml of α-terpineol to give a suspension. Then, the mixture was stirred for 3 h to get a homogenous suspension. Ethanol was subsequently removed via rotary evaporation to give a Bi_2WO_6 paste. Films were prepared doctor-blading on FTO. After each layer of paste was coated, the film was heated at 80 °C for 10 min before the next layer was applied. A total of three

layers of paste were used for both samples. Afterward, the films were sintered at 500 °C for 30 min, and then cooled to room temperature.

Dye absorption was carried out via immersing the films in an ethanol-based commercial N3 dye (Sigma-Aldrich) solution for 3 day. Then, the solar cells were assembled by using Ag/AgCl electrode, Pt wire and Bi_2WO_6 films as reference electrode, counter electrode and working electrode, respectively. The electrolyte is 0.2 M $HClO_4$ solution. The cell was degassed for 20 minutes by flushing Ar prior to each measurement. The electrode was illuminated with a 300W Xe lamp equipped with filters with cut-off of 420 nm. The linear sweep voltammetry (LSV) and chrono amperometry was monitored on an Auto lab.

3. Results and discussion

3.1 Structure, microstructure and optical property investigation.

The microstructure and morphology of bulk Bi_2WO_6 and single-unit-cell Bi_2WO_6 (SUC-Bi_2WO_6) samples are first investigated by SEM and TEM. As shown in Fig. 1a and b, both Bi_2WO_6 and SUC-Bi_2WO_6 display hierarchical microsphere structure with several microns in size, which is composed of plenty of nanosheets. From Fig. 1c, it is seen that the Bi_2WO_6 nanoplates are complanate and smooth with thickness of ~20 nm. In contrast, SUC-Bi_2WO_6 nanosheets are obviously curly and thin (Fig. 1d). From the TEM images (Fig. 1e and f), one can see the transparent nanosheets, indicating that the ultra-thin Bi_2WO_6 nanosheets are synthesized, and some single-layer nanosheets can be directly observed. The HRTEM image demonstrates two sets of lattice fringes with interplanar spacing of 0.272 nm, which correspond to the (200) and (020) planes of orthorhombic Bi_2WO_6. It reveals that the exposed facet of Bi_2WO_6 nanosheets is {001} facet, consistent

with the fast Fourier transformation (FFT) pattern (inset of Fig. 1f). Fig. 1g and h show the atomic force microscopic (AFM) images and the corresponding height profiles (inset) of SUC-Bi_2WO_6 nanosheets. They demonstrate that the thickness of SUC-Bi_2WO_6 nanosheets is 1.6 nm, which is in accordance with the thickness of an unit cell of Bi_2WO_6 (1.64 nm) along the [001] direction. These results disclose that the 3D Bi_2WO_6 microspheres constructed by nanosheets with well-defined single-unit-cell layer are successfully prepared via the one-pot SDBS-assisted hydrothermal reaction.

According to the above observations, the formation mechanism of the single-unit-cell layer assembled Bi_2WO_6 3D hierarchical architectures was proposed as illustrated in Scheme 1. Initially, the Bi^{3+} ion interacted with DBS^- ions to form Bi-DBS complexes via electrostatic interaction. This action should be in favor of impeding the hydrolysis of Bi^{3+} and thus facilitates its dispersion in the solution. Then, the Bi-DBS complexes react with WO_4^{2-} to generate Bi_2WO_6 nanosheets. Owing to the capping reagent effect from the long chain adsorbed on Bi^{3+}, the Bi_2WO_6 nanosheet is separately dispersed in the aqueous system, and then self-assembled into microspheres for reducing the surface energy [8].

DFT calculation was first employed to understand the difference in structure and optical properties between bulk Bi_2WO_6 and SUC-Bi_2WO_6. The models of single-unit-cell Bi_2WO_6 with different exposing atoms, namely, Bi exposed surface, O exposed surface 1 (from WO_6 octahedra and Bi_2O_2 slice), coplanar W-O exposed surface and O exposed surface 2 (from Bi_2O_2 slice), are illustrated in Fig. 2a. The surface energy of these models with and without consideration of van der Waals (VDW) force between Bi_2O_2 slices and W-O layers is calculated and the results are shown in Fig. 2b and c, respectively. It is obvious that no matter with or without consideration of VDW force, the surface energies of

the single-unit-cell Bi_2WO_6 with O exposed surface 1 and O exposed surface 2 are much lower than that of W-O co-exposed surface and Bi exposed surface. It indicates that the single-unit-cell Bi_2WO_6 with O exposed surface is more thermodynamically stable. For the above two kinds of O-exposed surface, the O exposed surface 1 has a lower surface energy with consideration of VDW. Thus, the single-unit-cell Bi_2WO_6 is more likely exists with O exposed surface 1. As shown in 2d and e, the O1 exposed single-unit-cell actually has two types of exposing O atoms, that is O atom from WO_6 octahedra and O atom from Bi_2O_2 slices. In contrast, the O2 exposed single-unit-cell only has one type of O atom, which is from Bi_2O_2 slices. Therefore, it is anticipated to determine which kind of O exposing by experimental methods, such as XPS.

XRD patterns of Bi_2WO_6 and SUC-Bi_2WO_6 are shown in Fig. 3a. All the diffraction peaks can be readily indexed into the orthorhombic-phase Bi_2WO_6 (JCPDS No. 73-2020), indicating that these samples are pure phase of Bi_2WO_6. Remarkably, the diffraction peaks of SUC-Bi_2WO_6 are obviously broadened and decreased in intensity compared to that of bulk Bi_2WO_6. This phenomenon should be attributed to the synergic effect of nanosize and microstrain effect of modified samples, namely, the Bi_2WO_6-SDBS products consist of thinner nanosheets, which is consistent with formation of single-unit-cell Bi_2WO_6 and above SEM, TEM and AFM results. Fig. 3b shows the Raman spectra of Bi_2WO_6 and SUC-Bi_2WO_6. The peaks at 827 and 795 cm^{-1} are separately associated with the antisymmetric and symmetric Ag modes of terminal O-W-O. The antisymmetric bridging mode of tungstate chain is indicated by the band at 713 cm^{-1}, and the peak at 306 cm^{-1} is assigned to the translational mode of simultaneous motions of Bi^{3+} and WO_6^{6-}

[25]. It can be seen that the difference between two samples is not very big, and the slight shift of Raman peaks may be resulted from the exposure of more atoms of SUC-Bi_2WO_6.

X-ray photoelectron spectroscopy (XPS) was utilized herein to investigate the change on coordination environment of each atom. Typical survey XPS spectra in Fig. 4a reveal that Bi, W and O elements can all be detected. In contrast to bulk Bi_2WO_6, the SUC-Bi_2WO_6 not only contains the characteristic Bi $4f_{5/2}$ and Bi $4f_{7/2}$ peaks at 164.8 and 159.5 eV, respectively [15], but also has two extra peaks at 165. 3 and 160.0 eV (Fig. 4b). The newly-appeared Bi peaks at higher binding energies imply that Bi atoms have a stronger coordination, which should be from the bonding with surface DBS^-. Similarly, in the W4f high resolution spectra (Fig. 4c), the two strong bands at 37.9 and 35.8 eV can be assigned to W $4f_{5/2}$ and W $4f_{7/2}$, respectively, and two new peaks occur at 38.4 and 36.2 eV. It also suggests a bonding effect between W atoms and surface DBS^- ions. These phenomena occurred for W and Bi indicate that the single-unit-cell Bi_2WO_6 has two types of exposed O atoms, which are from WO_6 octahedra and Bi_2O_2 slices, in good accordance with the above DFT results. Remarkably, it demonstrates that some O atoms are escaped from the surface, thus resulting in the exposure of Bi and W atoms. In other words, oxygen defect formed on the surface of SUC-Bi_2WO_6. Fig. 4d shows the O 1s spectra. They can be deconvoluted into three bands at 530.4, 531.1 and 532.5 eV, which are ascribed to lattice oxygen, hydroxyl groups and H_2O molecules adsorbed on the surface [34]. Compared with bulk Bi_2WO_6, SUC-Bi_2WO_6 has an evidently higher -OH amount, further confirming the abundant surface O atoms. Besides, more -OH can enable SUC-Bi_2WO_6 more hydrophilic, benefiting for photocatalytic reaction.

To get more information on the local structure evolution, XAFS data on the Bi L3-edge (13.419 keV) of bulk Bi_2WO_6 and SUC-Bi_2WO_6 were collected at room temperature. As shown in Fig. 5a, the Bi L-edge oscillation curves of bulk Bi_2WO_6 and SUC-Bi_2WO_6 present remarkable difference in the energy range of 13440-13540 eV, which demonstrates the different local atomic arrangements in the catalysts. Fig. 5b shows the Fourier transform (FT) curves of XAFS data. As it can be seen, there are mainly three peaks in the range from 1 to 4 Å, which corresponds to Bi-O, Bi-Bi and Bi-W distances, respectively. Notably, the radial distance of intrastratal Bi-O at 2.80 Å shows a shift (0.07 Å) to a higher value, which may be due to that Bi has a higher coordination with some other species adsorbed on surface, e.g. DBS^- anion. While for Bi-Bi and Bi-W bonds, compared to their distances (2.93 Å and 2.63 Å, respectively) in bulk Bi_2WO_6, obvious shift to small distance was observed. The shorter Bi-Bi and Bi-W bonds should be attributed to the absence of lattice O, namely, the generation of O defect. These observations are well consistent with the above XPS results.

To reflect the DBS^- anions on SUC-Bi_2WO_6, TG curves of Bi_2WO_6 and SUC-Bi_2WO_6 were measured with range of 20-600 °C, which covers the decomposition temperature of organics, and the results are shown in Fig. S2. It is obvious to see that both Bi_2WO_6 and SUC-Bi_2WO_6 are stable and show very similar TG curves. As revealed from the enlarged TG plots (inset of Fig. S2), SUC-Bi_2WO_6 presents a slightly larger decline in weight than Bi_2WO_6 with increasing the temperature, approximately 0.3%. It indicates that there may be a very tiny amount of DBS^- anions adsorbed on SUC-Bi_2WO_6. This is in accordance with the finding in above XAFS measurement. In view of the trace amount of SDBS, it should have a negligible effect on photocatalytic performance.

Microstructure change would produce a large effect on the specific surface area. As shown in Fig. 6a, the BET surface area of SUC-Bi2WO6 is 55.1 m^2/g, which is almost 2 times that of bulk Bi_2WO_6 (28.2 m^2/g). The enhanced surface area is expected to be beneficial to photocatalytic reaction.

The light absorption of Bi_2WO_6 and SUC-Bi_2WO_6 is investigated by UV-Vis diffuse reflectance spectra (DRS), as shown in Fig. 6b. In comparison to Bi_2WO_6 with an absorption edge of 450 nm, SUC-Bi_2WO_6 displays an obvious blue-shift of absorption edge (about 20 nm), which is attributed to the nano-sizing (NS) effect [35]. Correspondingly, the band gap of Bi_2WO_6 and SUC-Bi_2WO_6 is determined from transformed DRS to be 2.68 and 2.79 eV. It accords with blue-shift of the absorption edge. The band structures of Bi_2WO_6 and SUC-Bi_2WO_6 are studied by VB XPS and Mott-Schottky plot. As shown in Fig. 6c and d, the VB potentials for Bi_2WO_6 and SUC-Bi_2WO_6 are determined to be 1.89 and 1.95 eV, respectively. According to the band gaps of Bi_2WO_6 (2.68 eV) and SUC-Bi_2WO_6 (2.79 eV), the CB position of SUC-Bi_2WO_6 is supposed to be more negative than Bi_2WO_6. For confirmation, Mott–Schottky method is employed to elucidate the band energy potentials. Mott–Schottky plots (Fig. S3) demonstrated that the flat band potentials of Bi_2WO_6 and SUC-Bi_2WO_6 are -0.84 and -0.89 eV, respectively, versus a saturated calomel electrode (SCE). They are equal to -0.60 V and -0.65 V vs. a normal hydrogen electrode (NHE). The positive slope of $1/C^2$ versus potential curves indicates the n-type semiconductor feature of Bi_2WO_6 and SUC-Bi_2WO_6, which have a CB level of 0.1-0.3 eV higher than the flat band potential. Thus, the CB levels of Bi_2WO_6 and SUC-Bi_2WO_6 are roughly estimated to be -0.75 and -0.80 eV, and their VB positions are determined to be 1.93 and 1.99 eV, respectively. Therefore, compared to Bi_2WO_6, SUC-Bi_2WO_6 possesses

more negative CB positions and more positive VB position, which allow it to illustrate more powerful photo-redox driving force.

3.2 Selective adsorption and photocatalytic performance.

To systematically investigate the performance of SUC-Bi_2WO_6, the adsorption and photodegradation properties of Bi_2WO_6 are first monitored. Various organic contaminants with different charges are chose as molecular probes to study the selective adsorption ability. In our dye adsorption and degradation experiments, the pH value of reaction solutions is determined to be ~7. At this pH value, the dyes are ionisated according to their composition of anions and cations. For Rhodamine B (RhB), $C_{28}H_{31}ClN_2O_3=C_{28}H_{31}N_2O_3^+ + Cl^-$; For methylene blue (MB), $C_{16}H_{18}ClN_3S= C_{16}H_{18}N_3S^+ + Cl^-$; For methyl orange (MO), $C_{14}H_{14}N_3SO_3Na=C_{14}H_{14}N_3SO_3^- + Na^+$. Thus, RhB and MB are positively charged, while MO is negatively charged, as presented in Fig. 7a. To provide deep understanding on different substrate-catalyst interaction, the point of zero charge (PZC) of SUC-Bi_2WO_6 is measured. As shown in the Fig. S4, the PZC of SUC-Bi_2WO_6 is determined to be 4.34. Thus, SUC-Bi_2WO_6 is negatively charged when it was in the reaction solutions with a pH value of 7. Fig. 7b shows the adsorption curves of the four contaminants over SUC-Bi_2WO_6. It is obvious that the positively charged MB and RhB reveal an overwhelming desorption ability compared to the negatively charged MO and neutral phenol. This result further verifies the O exposure on the surface of single-unit-cell Bi_2WO_6. As illustrated in Fig. 7c, dye with positive charge could quickly adsorb on the surface O atoms due to the charge interaction, while negatively charged MO and neutral phenol show slight adsorption.

The photodegradation performance was studied by degradation of RhB. With visible light irradiation ($\lambda > 420$ nm) in the absence of catalyst, no RhB degradation was observed, indicating that RhB is stable under visible light (Fig. S5). As seen from Fig. 7d, in in addition to the increased adsorption ability, SUC-Bi_2WO_6 also presents a promoted photocatalytic degradation activity. The absorbance spectra of RhB over SUC-Bi_2WO_6 under visible-light with different illumination time were shown in Fig. S6. The main absorption peak of RhB at 554 nm shows a gradual shift to lower wavelength with prolonging the irradiation time, which indicates the occurence of de-ethylation process of the RhB dye [36]. After 0.5 h adsorption and 1 h light irradiation, the RhB removal ratio over SUC-Bi_2WO_6 is up to 93.1%, which is much higher than that of bulk Bi_2WO_6 (49.8%). This indicates that both adsorption and photodegradation performance are improved. Active species trapping experiment was conducted over SUC-Bi_2WO_6 in the RhB photodegradation process (Fig. S7). The addition of EDTA-2Na and BQ shows a great inhibition effect on RhB degradation, which demonstrated that holes and superoxide radicals ($\bullet O_2^-$) are the dominating active species for RhB photodegradation. The effect of SDBS concentration on the adsorption and removal of RhB is investigated. As shown in Fig, 7e, the adsorption and removal rates of RhB are decreased with increase of SDBS concentration, implying that more DBS^- adsorbed on the surface of Bi_2WO_6 is unfavourable for adsorption. It also demonstrates that the adsorption performance on positively-charged dye originates mainly from exposed O atoms. Moreover, sodium dodecyl sulfate (SDS), a similar anionic surface active agent to SDBS, is also employed to modify Bi_2WO_6. The XRD pattern of SDS modified Bi_2WO_6 (Fig. S8) shows similar broadened diffraction peak with decreased intensity in comparison with that of bulk Bi_2WO_6, which may reflect the prepa-

ration of ultra-thin Bi_2WO_6 nanosheets. The adsorption and photodegradation results reveal that SDS is more ineffective than SDBS. It may be due to that SDS has a shorter organic chain than SDBS, giving rise to formation of a relatively thicker layer of Bi_2WO_6 in the hydrothermal assembly process.

In order to further inspect the photocatalytic activity of single-unit-cell 3D Bi_2WO_6, photocatalytic water splitting into H_2 with methanol as sacrificial agent and Pt as co-catalyst was monitored. As shown in Fig. 8a, the SUC-Bi_2WO_6 displays remarkably enhanced photocatalytic H_2 evolution, and the H_2 production rate is up to 5.6 μmol/L (Fig. 8b), which is 14 times higher than that of bulk Bi_2WO_6 (0.4 μmol/L). It is worth noting that the current H_2 production rate is the highest among all the Bi_2WO_6 reported in the literature [31]. This result demonstrates that in addition to the improved photo-oxidation degradation the photo-reduction performance of Bi_2WO_6 could also be profoundly promoted by fabrication of single-unit-cell layer nanosheets established Bi_2WO_6 3D hierarchical architecture.

3.3 Systematic characterizations on photo-generated charge separation and transfer.

The enhanced photocatalytic performance of single-unit-cell Bi_2WO_6 is analysed by systematic photoelectrochemical measurements. Photocurrent response can indicate the interfacial charge generation and separation dynamics of a photoelectrode [37]. The photocurrent density-voltage (J-V) curves of Bi_2WO_6 and SUC-Bi_2WO_6 are presented in the Fig. 9a. With increase of potentials, the photocurrent density enhances for both electrodes. One can obviously see that SUC-Bi_2WO_6 produces largely enhanced photocurrent density compared to Bi_2WO_6 at different potentials, suggesting that SUC-Bi_2WO_6 should have a higher charge separation efficiency. It is reported that the J-V curve can indicate the den-

sity of charge carriers generated by photocatalysts in the presence of fast electron acceptor $MVCl_2$, as the onset potential of photocurrent in a voltammograms could determine the quasi Fermi level of majority carriers [38]. The relationship between quasi Fermi level and carrier density of Bi_2WO_6 and SUC-Bi_2WO_6 is elucidated according to the Nernst equation [39,40]:

$$E_{f1}-E_{f2}= kT\ln(N_{f1}-N_{f2})/e \quad (4)$$

where E_{f1} and E_{f2} are the quasi Fermi level of sample 1 and sample 2, N_{f1} and N_{f2} the carrier density, k the Boltzmann's Constant, T the temperature and e the elementary charge. As shown in Fig. 9b and its inset, the potential of Bi_2WO_6 and SUC-Bi_2WO_6 is -0.21 and -0.11 V, respectively. The difference of 0.1 V between the quasi Fermi levels of Bi_2WO_6 and SUC-Bi_2WO_6 demonstrates a 48 times carrier densities. In other words, SUC-Bi_2WO_6 produces a larger carrier density, which is 48-fold increase compared to Bi_2WO_6. Fig. 9c shows the transient photocurrent density of bulk Bi_2WO_6 and SUC-Bi_2WO_6 electrodes ($\lambda > 420$ nm) at 0.0 eV. Rapid generation of current with light on for both electrodes demonstrates that they are photo-sensitive. It is significant to note that their initial current densities can reach 0.6~0.8 μA when they are exposed to light, and then start to decay. The steady photocurrent of SUC-Bi_2WO_6 is approximately 4.77 μA, whereas a much greater current decay occurred for Bi_2WO_6 with only a steady photocurrent of 1.15 μA maintained. It indicates that Bi_2WO_6 has a higher recombination of electrons and holes than SUC-Bi_2WO_6. Namely, more efficient charge separation happens on the surface of SUC-Bi_2WO_6.

To further confirm the improved charge separation efficiency of SUC-Bi_2WO_6, photocurrent density of bulk Bi_2WO_6 and SUC-Bi_2WO_6 electrodes is monitored under light

irradiation with different wavelengths, including 420 nm, 450 nm, 500 nm, 550 nm and 600 nm. As shown in Fig. 9d, it is evident that the photocurrent of SUC-Bi_2WO_6 is all much higher than that of Bi_2WO_6 at the above wavelengths. This result further verifies the more efficient charge separation of SUC-Bi_2WO_6, which is not dependent on wavelengths of irradiation light.

Surface photovoltage (SPV) spectroscopy is an effective and convincing technique to reveal the photogenerated charge separation of excited states generated by absorption. The SPV signal is resulted from the surface potential barrier change before and after light irradiation. Thus, the SPV amplitude can reflect the charge separation extent in the corresponding photo-responsive range [41]. Fig. 10 displays the SPV spectra of bulk Bi_2WO_6 and SUC-Bi_2WO_6 samples. In comparison with bulk Bi_2WO_6, SUC-Bi_2WO_6 shows an obviously stronger SPV response in the range of 300-430 nm. The SPV provide a solid evidence that more efficient light-induced charge separation occurred in SUC-Bi_2WO_6 in contrast to bulk Bi_2WO_6.

3.4 Performance as dye-sensitized solar cells.

As the single-unit-cell Bi_2WO_6 has abundant exposed O atoms and increased surface area, it may have a good dye-sensitized photoelectrochemical property. Fig. 11a shows the schematic diagram of water-splitting dye-sensitized solar cell (WS-DSSC) mechanism of dye (N3) sensitized Bi_2WO_6 photoanode. When N3 is excited by light irradiation, photoinduced electrons will be produced. The electrons immediately migrate from the lowest unoccupied molecular orbital (LUMO) of N3 onto the conduction band (CB) of Bi_2WO_6, and then are transferred to the surface of ITO. The photocurrent density-voltage (J-V) curves of Bi_2WO_6 and SUC-Bi_2WO_6 photoanodes are shown in Fig. 11b. It is obvi-

ous to note that SUC-Bi_2WO_6 all presents much higher current density than SUC-Bi_2WO_6 at different potentials, and the current difference between Bi_2WO_6 and SUC-Bi_2WO_6 photoanodes gradually increases with raising the potential. Fig. 11c displays chrono amperometry of N3 sensitized Bi_2WO_6 and SUC-Bi_2WO_6 photoanodes at 0.9 V. They reveal swift current response with light on and off, and N3 sensitized SUC-Bi_2WO_6 photoanodes yields a highly strengthened current density, 16 $\mu A/cm^2$ on average, which is ~12 times that of Bi_2WO_6. After 500 s visible-light irradiation, the high current density of SUC-Bi_2WO_6 shows only slight decay, demonstrating the high stability and excellent photoelectrochemical performance of SUC-Bi_2WO_6 DSSC.

4. Conclusion

In summary, single-unit-cell layer assembled Bi_2WO_6 3D hierarchical architectures are fabricated by a sodium dodecyl benzene sulfonate (SDBS)-assisted assembled strategy. Experimental and DFT calculations results uncover that the exposed surface atoms are O atoms from Bi-O and W-O groups, and thus the single-unit-cell layer 3D Bi_2WO_6 shows strong selective adsorption on positively-charged organic dyes. It is also demonstrated that sodium dodecyl sulfate (SDS) is less effective that SDBS, which may be due to its shorter organic chains. The photocatalytic experiments disclose that the single-unit-cell layer 3D Bi_2WO_6 displays profoundly enhanced photodegradation activity and especially a prominent photocatalytic H_2 evolution rate, which is 14 times that of bulk Bi_2WO_6. The photocurrent and photovoltage measurements show that the remarkably strengthened photocatalytic performance is attributed to substantially promoted carrier density and charge separation efficiency in addition to increased surface area. Additionally, the sin-

gle-unit-cell layer 3D Bi_2WO_6 was demonstrated to be a potential dye-sensitized photoanode for oxygen evolution reaction (ORR). The study may provide a general and efficient protocol for developing single-layered materials for photocatalytic or photoelectrochemical applications.

Competing interest

The authors declare no competing financial interest.

Acknowledgement

This work was jointly supported by the National Natural Science Foundations of China (No. 51672258 and 51572246), the Fundamental Research Funds for the Central Universities (2652015296).

Appendix A. Supplementary data

Supplementary data associated with this article can be found,in the online version, at

References

[1] X.C. Wang, K. Maeda, A. Thomas, K. Takanabe, G. Xin, J.M. Carlsson, K. Domen, M. Antonietti, Nat. Mater. 8 (2009) 76-80.

[2] Q.H. Wang, K. Kalantar-Zadeh, A. Kis, J.N. Coleman, M.S. Strano, Nat. Nanotechnol. 7 (2012) 699-712.

[3] L.V. Lightcap, T.H. Kosel, P.V. Kamat, Nano. Lett. 10 (2010) 577-583.

[4] R.L. Bickley, G.C. Williams, Mater. Chem. Phys. 51 (1997) 47.

[5] H.F. Cheng, B.B. Huang, Y. Dai, Nanoscale. 6 (2014) 2009-2026.

[6] J. Li, Y. Yu, L.Z. Zhang, Nanoscale. 6 (2014) 8473-8488.

[7] H. Li, J. Shang, Z.H. Ai, L.Z. Zhang, J. Am. Chem. Soc. 137 (2015) 6393-6399.

[8] X. Zhang, Z.H. Ai, F.L. Jia, L.Z. Zhang, J. Phys. Chem. C 112 (2008) 747-753.

[9] X. Xiao, R. Hao, M. Liang, X.X. Zuo, J. M. Nan, L.S. Li, W.D. Zhang, J. Hazard. Mater. 122 (2012) 233-234.

[10] J. Cao, B.Y. Xu, H.L. Lin, B.D. Luo, S.F. Chen, Chem. Eng. J. 185-186 (2012) 91-99.

[11] H.W. Huang, K. Xiao, Y. He, T.R. Zhang, F. Dong, X. Du, Y.H. Zhang, Appl. Catal. B: Environ 199 (2016) 75-86.

[12] J. Bi, L. Wu, J. Li, Z. Li, X. Wang, X. Fu, Acta Mater. 55 (2007) 4699-4705.

[13] S.C. Zhang, C. Zhang, Y. Man, Y.F. Zhu, J. Solid State Chem. 179 (2006) 62-69.

[14] R.G. Chen, J.H. Bi, L. Wu, W.J. Wang, Z.H. Li, X. Z. Fu, Inorg. Chem. 48 (2009) 9072-9076.

[15] H.W. Huang, K. Liu, K. Chen, Y.L. Zhang, Y.H. Zhang, S.C. Wang, J. Phys. Chem. C 118 (2014) 14379-14387.

[16] X. Lin, T. Huang, F. Huang, W. Wang, J. Shi, J. Mater. Chem. 17 (2007) 2145-2150.

[17] Y. He, Y.H. Zhang, H.W. Huang, N. Tian, Y.X. Guo, Y. Luo, Colloids. Surf. A 462 (2014) 131-136.

[18] Z. Zou, J. Ye, H. Arakawa, J. Mol. Catal. A: Chem. 168 (2001) 289-297.

[19] H.W. Huang, Y. He, Z.S. Lin, L. Kang, Y.H. Zhang, J. Phys. Chem. C 117 (2013) 22986-22994.

[20] H.W. Huang, Y. He, X.W. Li, M. Li, C. Zeng, F. Dong, X. Du, T.R. Zhang, Y.H. Zhang, J. Mater. Chem. A 3 (2015) 24547-24556.

[21] X. Wang, J.C. Ran, M. Tao, Y. He, Y.H. Zhang, X.W. Li, H.W. Huang, Mater. Sci. in Semicon. Proc. 41 (2016) 317–322.

[22] H.W. Huang, S.B. Wang, Y.H. Zhang, X. Han, Mater. Res. Bull. 62 (2015) 206-211.

[23] Y. He, H.W. Huang, Y.H. Zhang, X.W. Li, N. Tian, Y.X. Guo, Y. Luo, Mater. Res. Bull. 64 (2015) 405-409.

[24] L. W. Zhang, Y. Man, Y.F. Zhu, ACS Catal. 1 (2011) 841-848.

[25] R. Shi, G.L. Huang, J. Lin, Y.F. Zhu, J. Phys. Chem. C 113 (2009) 19633-19638.

[26] J. Tian, Y.H. Sang, G.W. Yu, H.D. Jiang, X.N. Mu, H. Liu, Adv. Mater. 25 (2013) 5075-5080.

[27] D.Q. He, L.L. Wang, D.D. Xu, J.L. Zhai, D.J. Wang, T.F. Xie, ACS Appl. Mater. Interfaces 3 (2011) 3167–3171.

[28] Y.L. Tian, B.B. Chang, J.L. Lu, J. Fu, F.N. Xi, X.P. Dong, ACS Appl. Mater. Interfaces 5 (2013) 7079–7085.

[29] Z.J. Zhang, W.Z. Wang, E.P. Gao, S.M. Sun, L. Zhang, J. Phys. Chem. C 116 (2012) 25898-25903.

[30] J. Ren, W.Z. Wang, S.M. Sun, L. Zhang, J. Chang, Appl. Catal. B 92 (2009) 50.

[31] Y.G. Zhou, Y.F. Zhang, M.S. Lin, J.L. Long, Z.Z. Zhang, H.X. Lin, J.C.S. Wu, X.X. Wang, Nat. Comm. 6 (2015) 8340.

[32] L. Liang, F.C. Lei, S. Gao, Y.F. Sun, X.C. Jiao, J. Wu, S. Qamar, Y. Xie, Angew. Chem. Int. Ed. 54 (2015) 13971-13974.

[33] B. Ravel, M. Newville, J. Synchrotron Radiat. 12 (2005) 537-541.

[34] S. Guo, X.F. Li, H.Q. Wang, F. Dong, Z.B. Wu, J. Colloid Interf. Sci. 369 (2012) 373-380.

[35] M. Guan, C. Xiao, J. Zhang, S. Fan, R. An, Q. Cheng, J. Xie, M. Zhou, B. Ye, Y. Xie, J. Am. Chem. Soc. 135 (2013) 10411−10417.

[36] H.A. Ahsaine, M. Ezahri, A. Benlhachemi, B. Bakiz, S. Villain, F. Guinneton, J.R. Gavarri. 42 (2016) 8552-8558.

[37] H.W. Huang, X.W. Li, J.J. Wang, F. Dong, P.K. Chu, T.R. Zhang, Y.H. Zhang, ACS Catal. 5 (2015) 4094.

[38] Z.F. Hu, L.Y. Yuan, Z.F. Liu, Z.R. Shen, J.C. Yu, Angew. Chem. Int. Ed. 55 (2016) 9580-9585.

[39] P.M. Rao, L. Cai, C. Liu, I.S. Cho, C.H. Lee, J.M. Weisse, P. Yang, X. Zheng, Nano Letters. 14 (2014) 1099-1105.

[40] J. Zhao, M.A. Holmes, F.E. Osterloh, ACS Nano. 7 (2013) 4316-4325.

[41] J. Jiang, L.Z. Zhang, H. Li, W.W. He, J.J. Yin, Nanoscale 5 (2013) 10573-10581.

Scheme 1. Formation diagram of the single-unit-cell layer assembled Bi_2WO_6 3D hierarchical architectures.

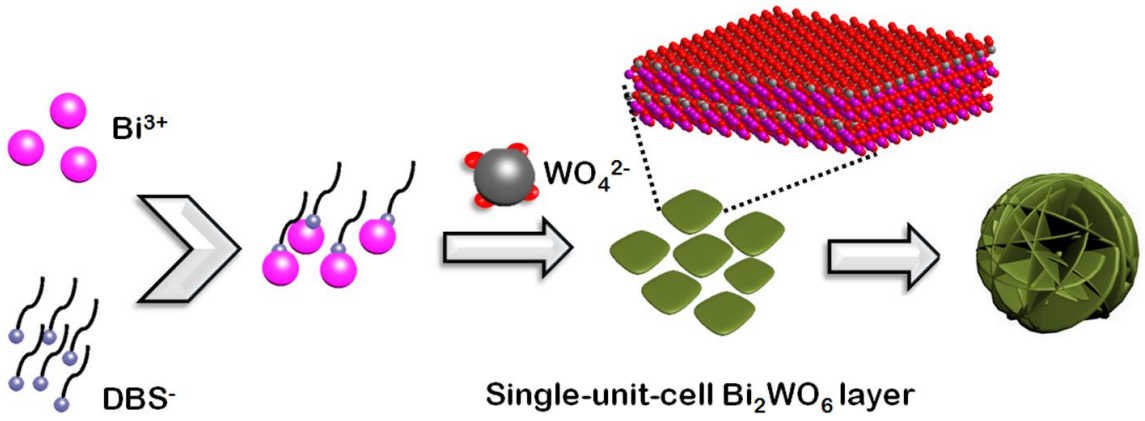

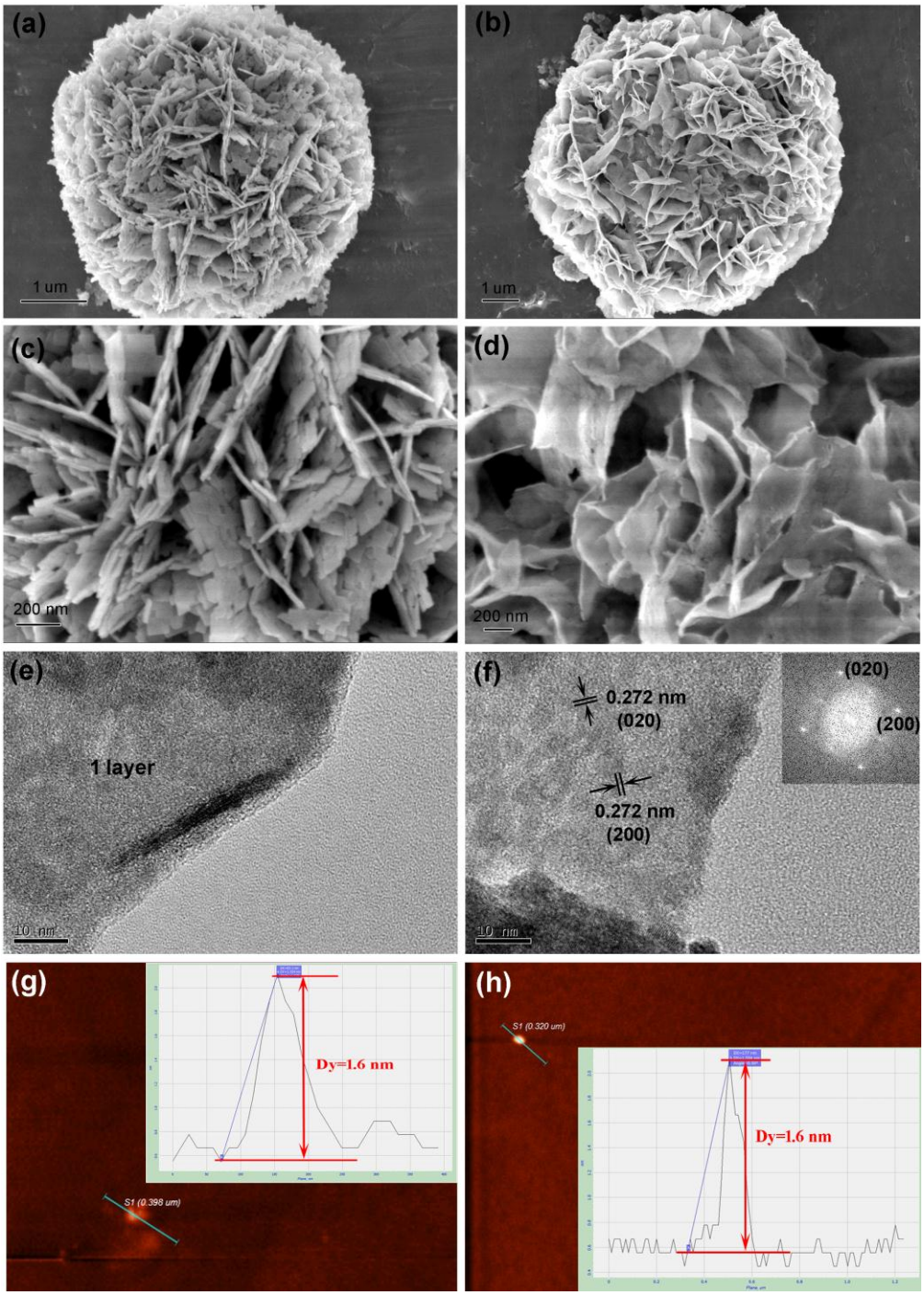

Fig. 1 SEM images of (a,c) Bi_2WO_6 and (b,d) SUC-Bi_2WO_6; (e,f) HR-TEM images, (g,h) AFM images and corresponding height profiles (insets) of SUC-Bi_2WO_6.

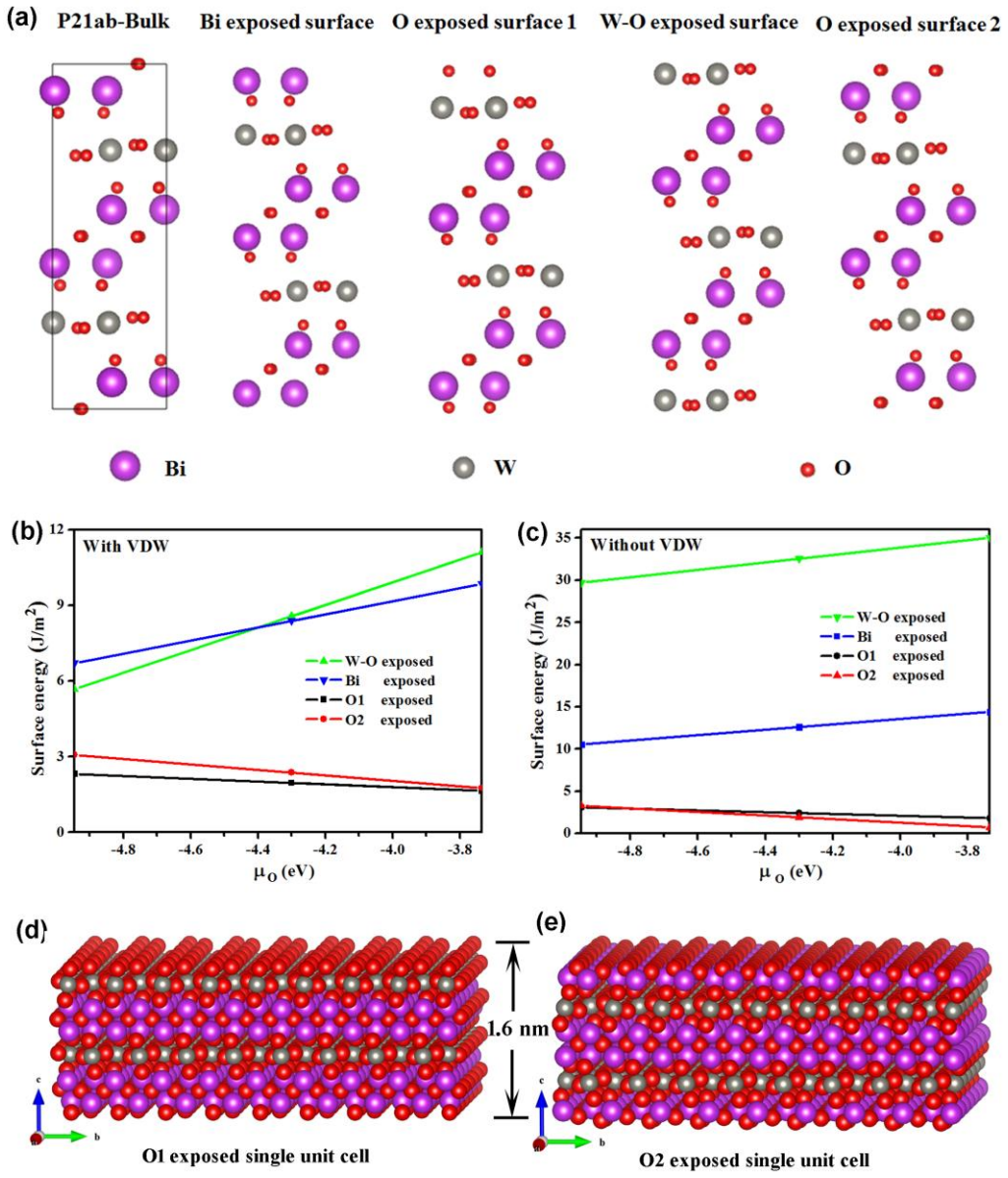

Fig. 2 (a) Crystal structure of bulk Bi_2WO_6 and SUC-Bi_2WO_6 with different surface exposing atoms. Surface energy of SUC-Bi_2WO_6 with different surface exposing atoms (b) with and (c) without consideration of van der Waals force. Crystal structure of (d) O1 exposed single unit cell and (e) O2 exposed single unit cell.

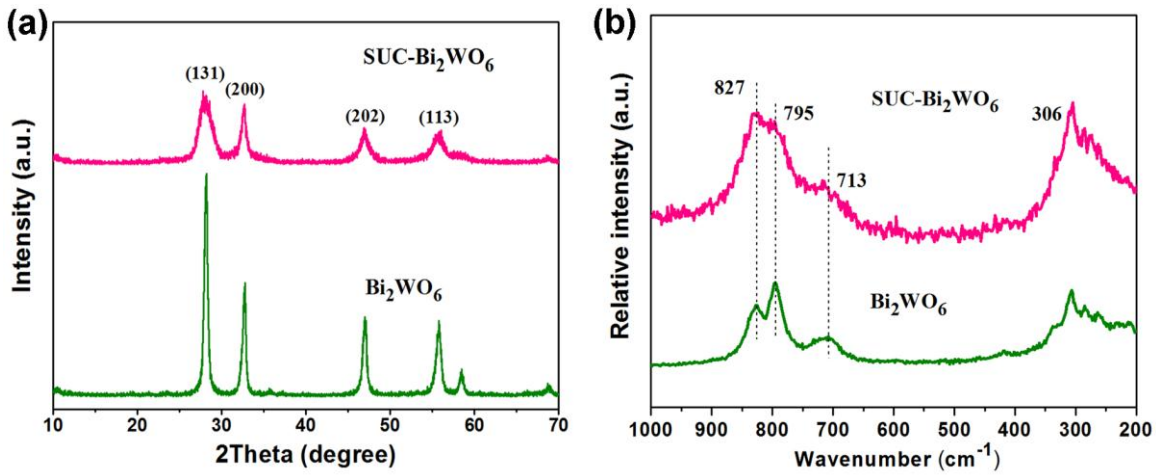

Fig. 3 (a) XRD patterns and (b) Raman spectra of Bi_2WO_6 and SUC-Bi_2WO_6.

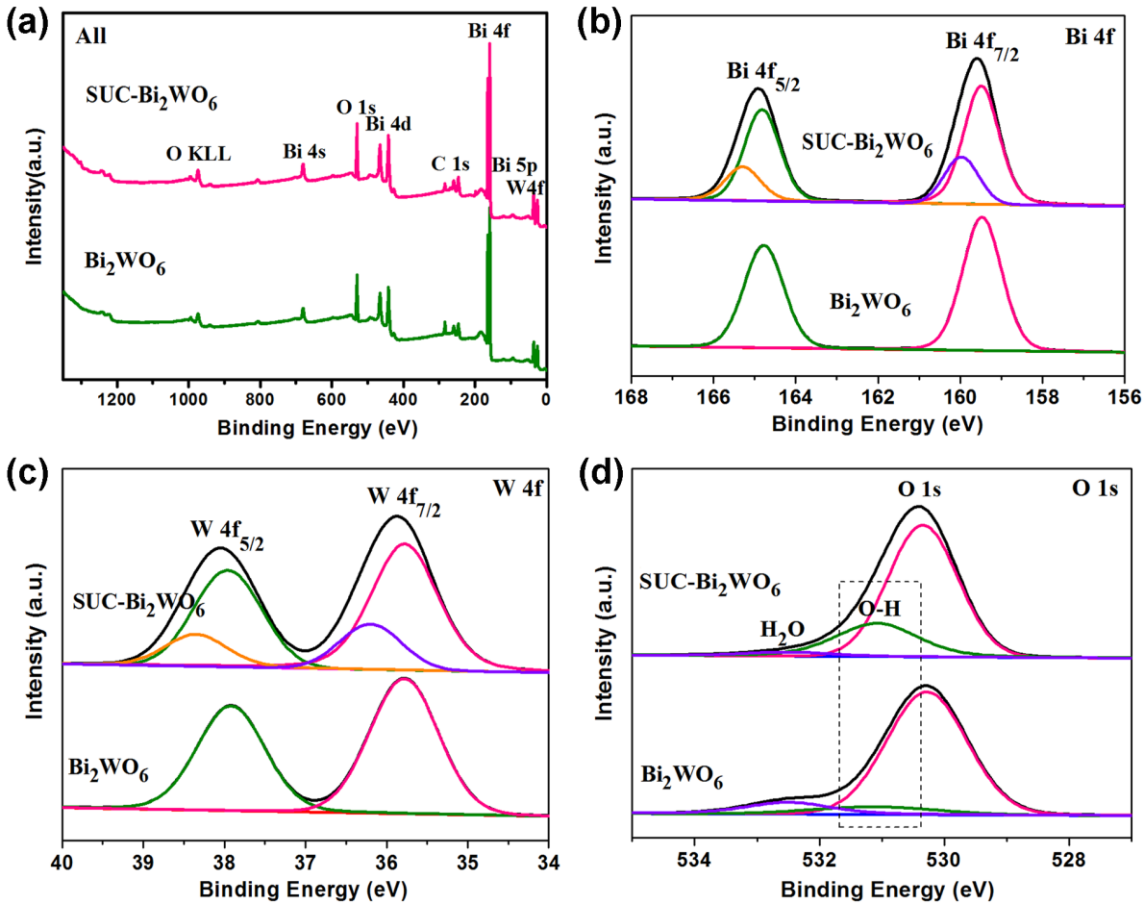

Fig. 4 (a) Survey XPS spectra, (b) High-resolution Bi 4f, (c) W 4f and (d) O 1s spectra of XPS spectra of Bi_2WO_6 and SUC-Bi_2WO_6.

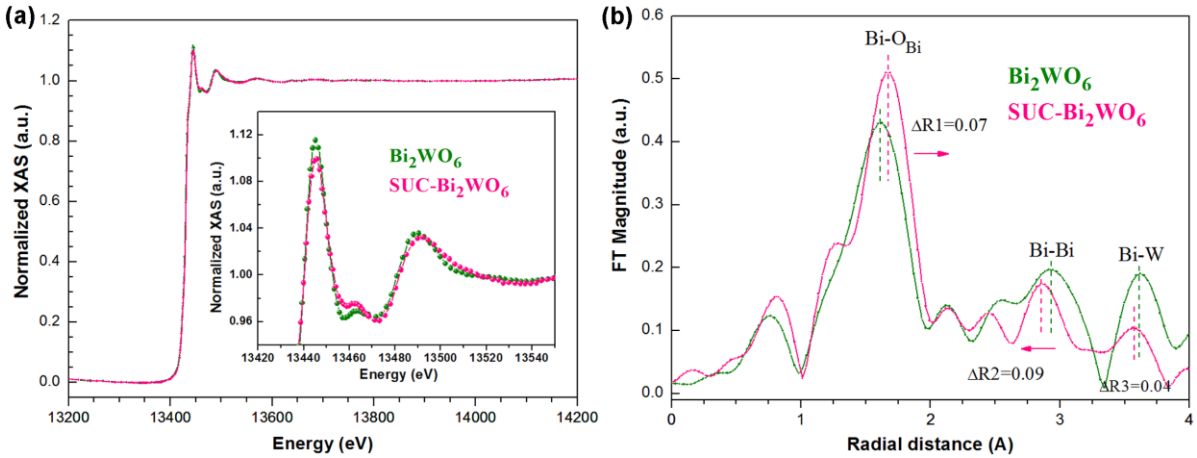

Fig. 5 (a) Normalized Bi L-edge XAFS spectra and (b) Fourier transformed profiles for Bi coordination environments of Bi_2WO_6 and SUC-Bi_2WO_6.

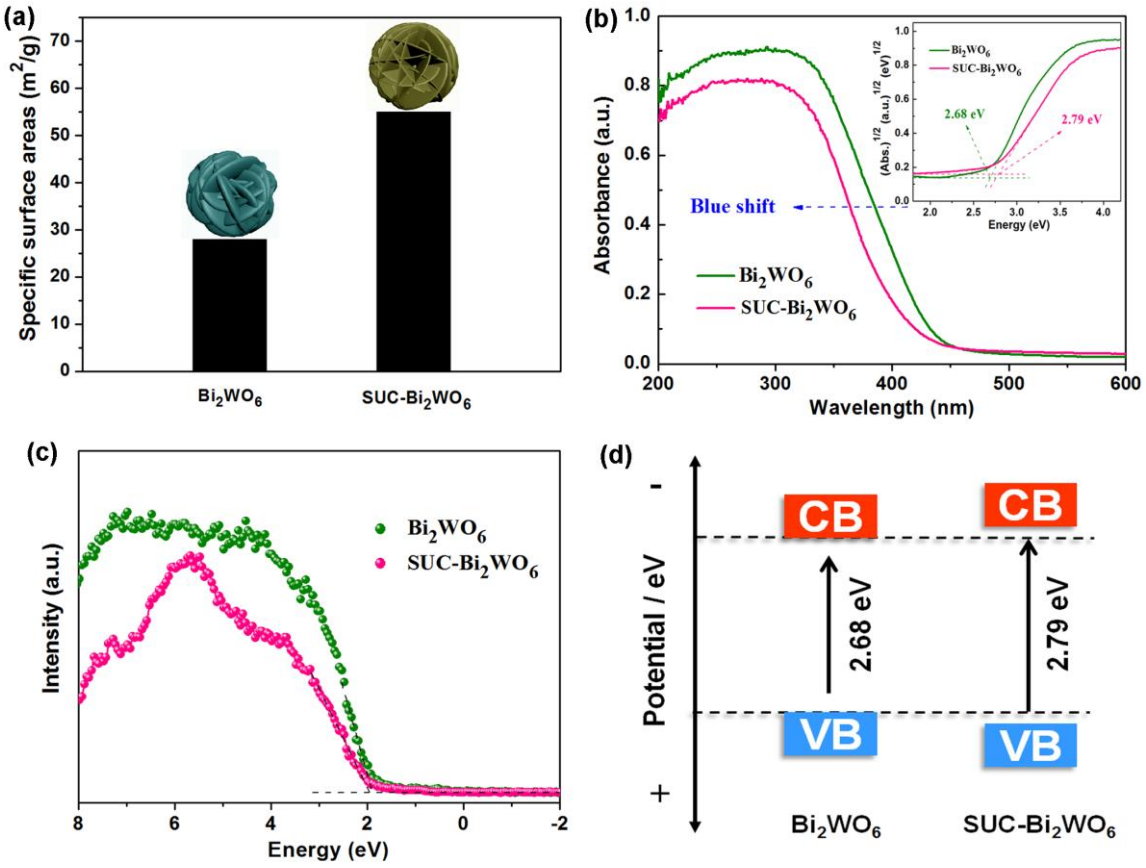

Fig. 6 (a) BET surface areas of Bi_2WO_6 and SUC-Bi_2WO_6 (b) UV-vis diffuse reflectance spectra (DRS) and band gap (inset) of Bi_2WO_6 and SUC-Bi_2WO_6. (c) VB XPS and (d) schematic band structures of Bi_2WO_6 and SUC-Bi_2WO_6

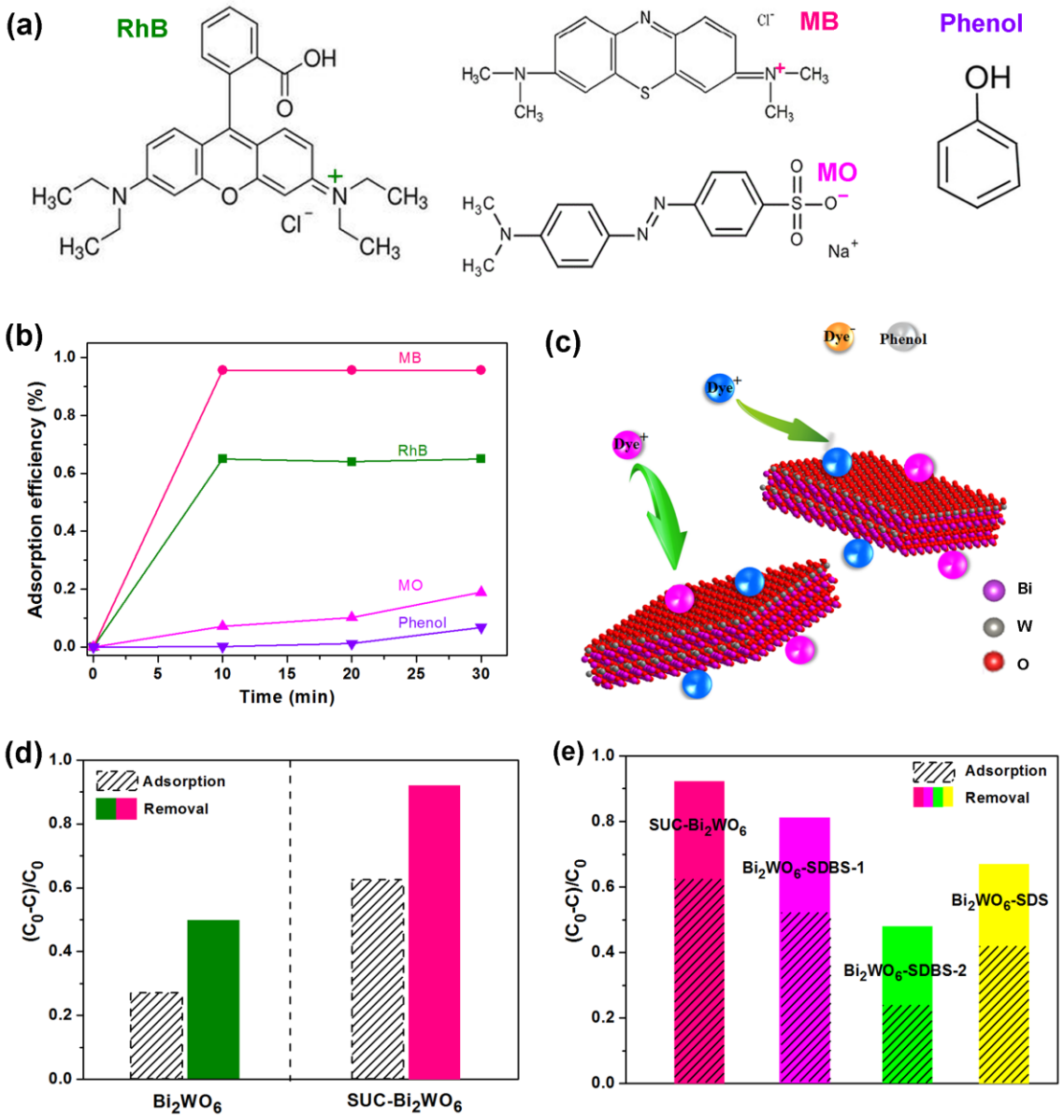

Fig. 7 (a) Molecular structures of RhB, MB, MO and phenol with their charges. (b) Adsorption curves of RhB, MB, MO and phenol over SUC-Bi_2WO_6 in darkness for 0.5 h. (c) Diagram illustration for adsorption of dyes on the surface of SUC-Bi_2WO_6. Adsorption efficiencies in darkness and removal efficiencies (including adsorption and photodegradation with visible light irradiation ($\lambda > 420$ nm)) of RhB over (d) Bi_2WO_6 and SUC-Bi_2WO_6 and (e) SUC-Bi_2WO_6, Bi_2WO_6-SDBS-1, Bi_2WO_6-SDBS-2 and Bi_2WO_6-SDS.

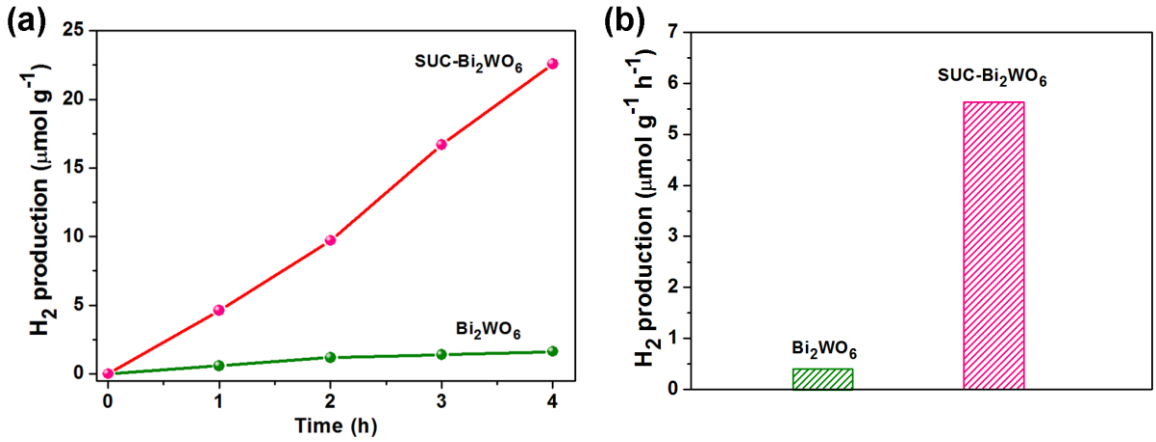

Fig. 8 (a) Photocatalytic H_2 production curves and (b) corresponding rates of Bi_2WO_6 and SUC-Bi_2WO_6 under visible light irradiation ($\lambda > 420$ nm).

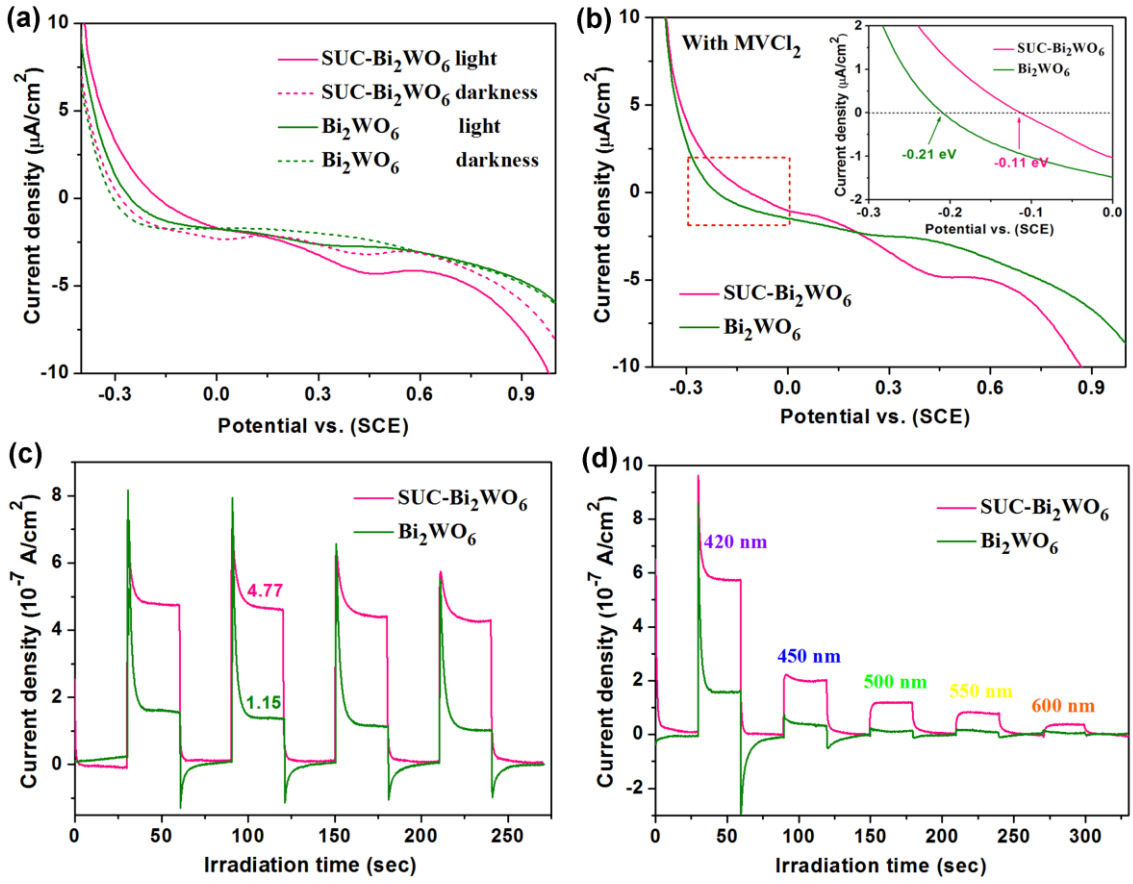

Fig. 9 Current density-voltage (J-V) curves of Bi_2WO_6 and SUC-Bi_2WO_6 under visible light irradiation ($\lambda > 420$ nm) ([Na_2SO_4] = 0.1 M) (a) with and (b) without methylviologen dichloride ($MVCl_2$). Transient photocurrent response of Bi_2WO_6 and SUC-Bi_2WO_6 (c) with visible light irradiation ($\lambda > 420$ nm) and (d) with different wavelengths.

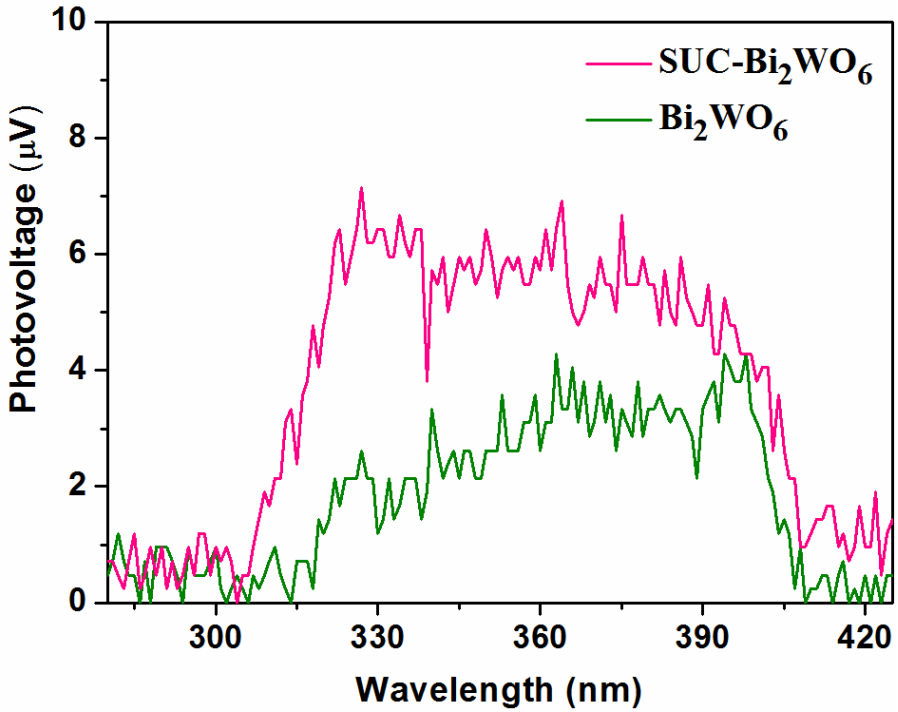

Fig. 10 SPV spectra of the Bi_2WO_6 and SUC-Bi_2WO_6.

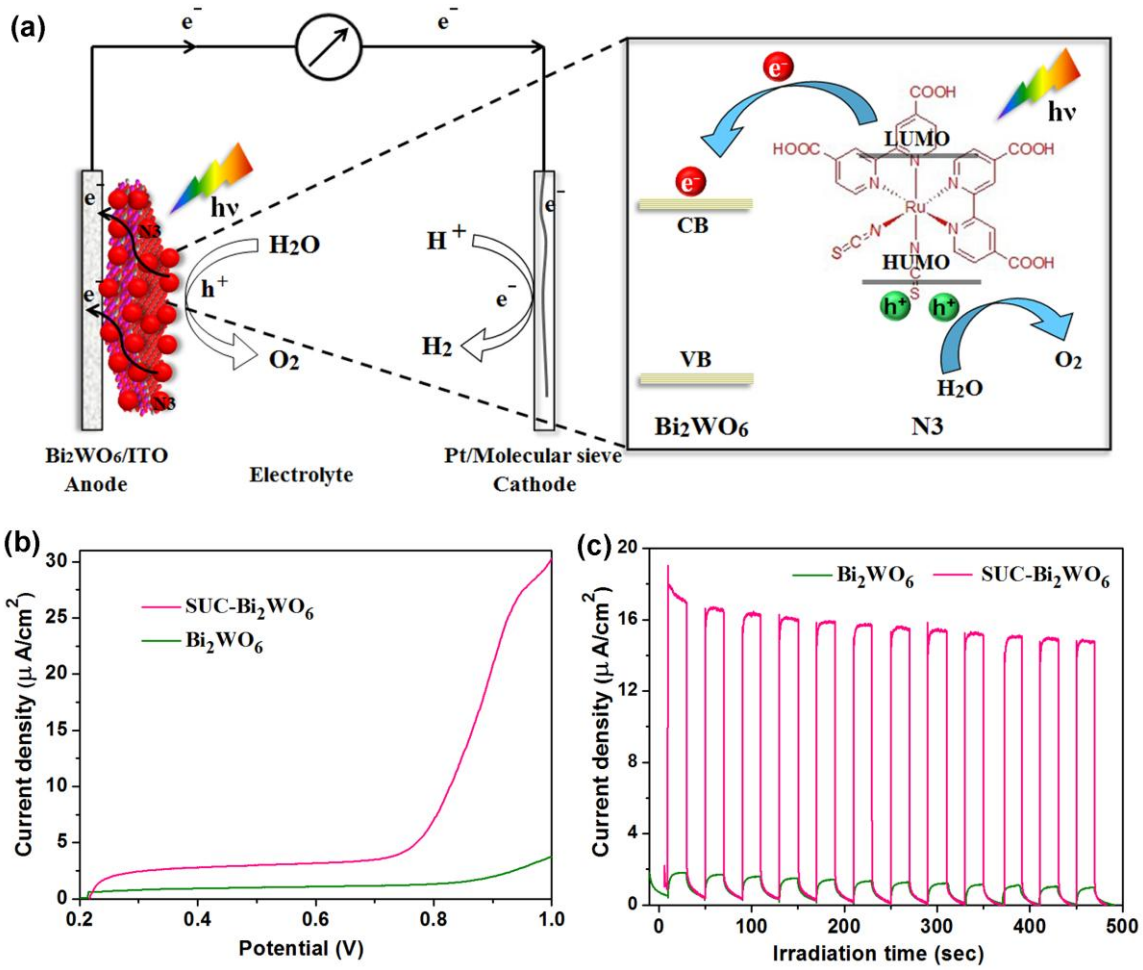

Fig. 11 (a) The schematic illustration of DSSC mechanism with a dye (N3) sensitized Bi_2WO_6 photoanode. (b) Current density-voltage (J-V) curves and (c) chrono amperometry of Bi_2WO_6 and SUC-Bi_2WO_6 at 0.9 V under visible light irradiation ($\lambda > 420$ nm).